The aerodynamics of revolving wings

I. Model hawkmoth wings

James R. Usherwood* and Charles P. Ellington

Department of Zoology, University of Cambridge, Downing Street, Cambridge CB2 3EJ, UK

*Present address: Concord Field Station, MCZ, Harvard University, Old Causeway Road, Bedford, MA 01730, USA
(e-mail: jimusherwood@lycos.co.uk)

Summary

Recent work on flapping hawkmoth models has demonstrated the importance of a spiral 'leading-edge vortex' created by dynamic stall, and maintained by some aspect of spanwise flow, for creating the lift required during flight. This study uses propeller models to investigate further the forces acting on model hawkmoth wings in 'propeller-like' rotation ('revolution'). Steadily revolving model hawkmoth wings produce high vertical ($\approx$ lift) and horizontal ($\approx$ profile drag) force coefficients because of the presence of a leading-edge vortex. Both horizontal and vertical forces, at relevant angles of attack, are dominated by the pressure difference between the upper and lower surfaces; separation at the leading edge prevents 'leading-edge suction'. This allows a simple geometric relationship between vertical and horizontal forces and the geometric angle of attack to be derived for thin, flat wings. Force coefficients are remarkably unaffected by considerable variations in leading-edge detail, twist and camber. Traditional accounts of the adaptive functions of twist and camber are based on conventional attached-flow aerodynamics and are not supported. Attempts to derive conventional profile drag and lift coefficients from 'steady' propeller coefficients are relatively successful for angles of incidence up to 50° and, hence, for the angles normally applicable to insect flight.

Key words: aerodynamics, *Manduca sexta*, propeller, hawkmoth, model, leading-edge vortex, flight, insect, lift, drag.

Introduction

Recent experiments on the aerodynamics and forces experienced by model flapping insect wings have allowed great leaps in our understanding of the mechanisms of insect flight. 'Delayed stall' creates a leading-edge vortex that accounts for two-thirds of the required lift during the downstroke of a hovering hawkmoth (Ellington et al., 1996; Van den Berg and Ellington, 1997b). Maxworthy (1979) identified such a vortex during the 'quasi-steady second phase of the fling' in a flapping model, but its presence and its implications for lift production by insects using a horizontal stroke plane have only been realised after the observations of smoke flow around tethered (Willmott et al., 1997) and mechanical (Van den Berg and Ellington, 1997a,b) hawkmoths. Additional mechanisms, 'rotational circulation' (referring to rotation about the pronation/supination axis) and 'wake capture', described for a model *Drosophila*, account for further details of force production, particularly important in control and manoeuvrability (Dickinson et al., 1999; Sane and Dickinson, 2001).

Experiments based on flapping models are the best way at present to investigate the unsteady and three-dimensional aspects of flapping flight. The effects of wing–wing interaction, wing rotation about the supination/pronation axis, wing acceleration and interactions between the wing and the induced flow field can all be studied with such models. However, experiments with flapping models inevitably confound some or all of these variables. To investigate the properties of the leading-edge vortex over 'revolving' wings, while avoiding confounding effects from wing rotation (pronation and supination) and wing–wing interaction, this study is based on a propeller model. 'Revolving' in this study refers to the rotation of the wings about the body, as in a propeller. The conventional use of the term 'rotation' in studies of insect flight, which refers to pronation and supination, is maintained. A revolving propeller mimics, in effect, the phase of a down- (or up-) stroke between periods of wing rotation.

The unusually complete kinematic and morphological data available for the hovering hawkmoth *Manduca sexta* (Willmott and Ellington, 1997b), together with its relatively large size, have made this an appropriate model insect for previous aerodynamic studies. This, and the potential for comparisons with computational (Liu et al., 1998) and mechanical flapping models, both published and current, make Willmott and Ellington's (1997b) hovering hawkmoth an appropriate starting point for propeller experiments.

This study assesses the influences of leading-edge detail, twist and camber on the aerodynamics of revolving wings. The

similarities between the leading-edge vortex over flapping wings and those found over swept and delta wings operating at high angles of incidence (Van den Berg and Ellington, 1997b) suggest that the detail of the leading edge may be of interest (Lowson and Riley, 1995): the sharpness of the leading edge of delta wings is critical in determining the relationship between force coefficients and angle of attack. Protuberances from the leading edge are used on swept-wing aircraft to delay or control the formation of leading-edge vortices (see Ashill et al., 1995; Barnard and Philpott, 1995). Similar protuberances at a variety of scales exist on biological wings, from the fine sawtooth leading-edge of dragonfly wings (Hertel, 1966) to the adapted digits of birds (the alula), bats (thumbs) and some, but not all, sea-turtles and pterosaurs. The effect of a highly disrupted leading edge is tested using a 'sawtooth' variation on the basic hawkmoth planform.

Willmott and Ellington (1997b) observed wing twists of 24.5° (downstroke) to 19° (upstroke) in the hovering hawkmoth F1, creating higher angles of attack at the base than at the tip for both up- and downstroke. Such twists are typical for a variety of flapping insects (e.g. Jensen, 1956; Norberg, 1972; Weis-Fogh, 1973; Wootton, 1981; Ellington, 1984c), but this is not always the case (Vogel, 1967a; Nachtigall, 1979). The hawkmoth wings were also seen to be mildly cambered, agreeing with observations for a variety of insects; see, for instance, photographs by Dalton (1977) or Brackenbury (1995). Both these features of insect wings have been assumed to provide aerodynamic benefits (e.g. Ellington, 1984c) and have been shown to be created by largely passive, but intricate, mechanical deflections (Wootton, 1981, 1991, 1992, 1993, 1995; Ennos, 1988).

Previous studies of the effects of camber have had mixed results. Camber on conventional aircraft wings increases the maximum lift coefficients and normally improves the lift-to-drag ratio. This is also found to be true for locust (Jensen, 1956), *Drosophila* (Vogel, 1967b) and bumblebee (Dudley and Ellington, 1990b) wings. However, the effects of camber on unsteady wing performance appear to be negligible (Dickinson and Götz, 1993).

The propeller rig described here enables the aerodynamic consequences of leading-edge vortices to be studied. It also allows the importance of various wing features, previously described by analogy with conventional aerofoil or propeller theory, to be investigated.
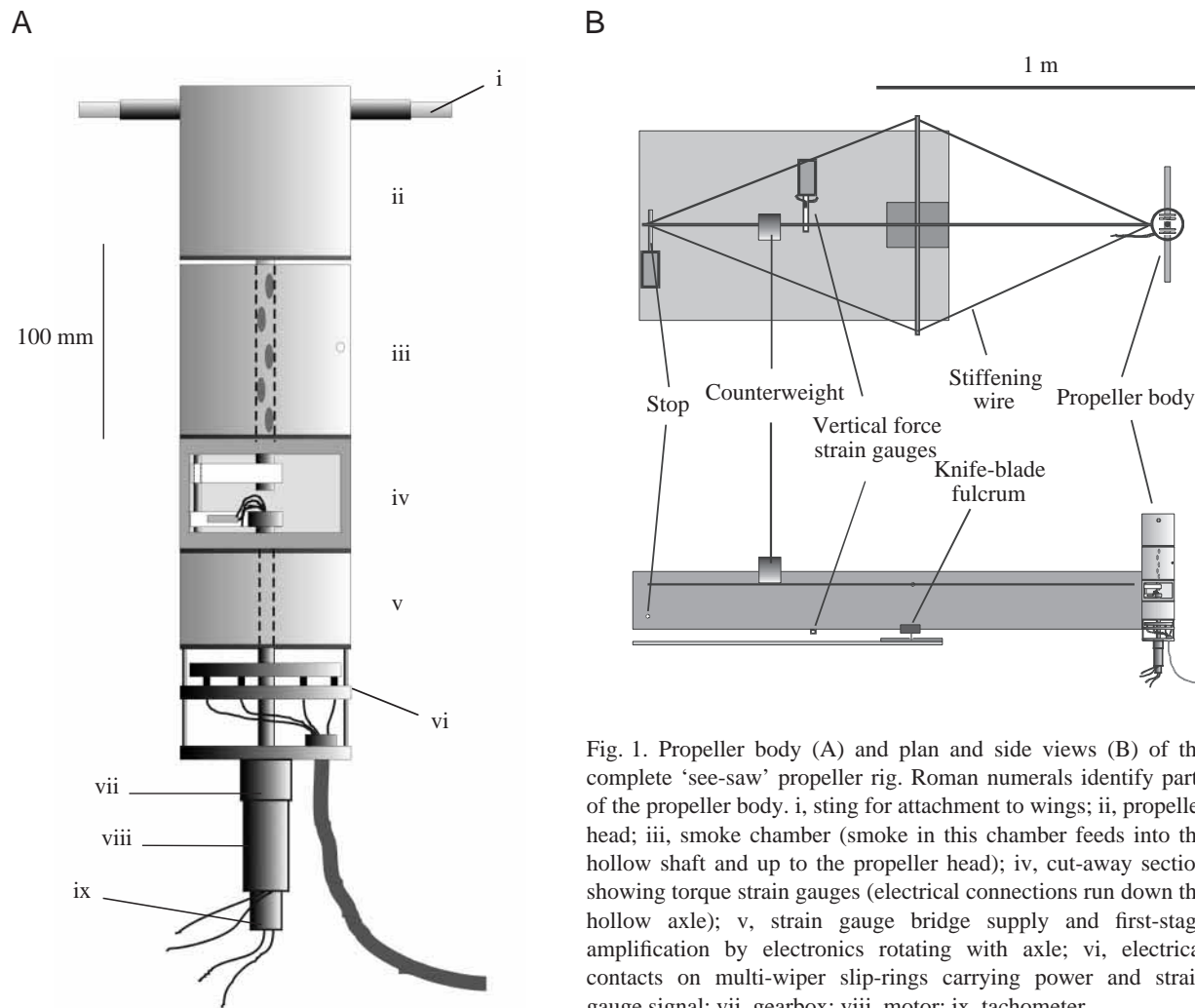

Fig. 1. Propeller body (A) and plan and side views (B) of the complete 'see-saw' propeller rig. Roman numerals identify parts of the propeller body. i, sting for attachment to wings; ii, propeller head; iii, smoke chamber (smoke in this chamber feeds into the hollow shaft and up to the propeller head); iv, cut-away section showing torque strain gauges (electrical connections run down the hollow axle); v, strain gauge bridge supply and first-stage amplification by electronics rotating with axle; vi, electrical contacts on multi-wiper slip-rings carrying power and strain gauge signal; vii, gearbox; viii, motor; ix, tachometer.

Materials and methods

The experimental propeller

A two-winged propeller (Fig. 1) was designed and built to enable both the quantitative measurement of forces and the qualitative observation of the flows experienced by propeller blades (or 'wings') as they revolve.

The shaft of the propeller was attached *via* a 64:1 spur gearbox to a 12 V Escap direct-current motor/tachometer driven by a servo with tachometer feedback. The input voltage was ramped up over 0.8 s; this was a compromise between applying excessive initial forces (which may damage the torque strain gauges and which set off unwanted mechanical vibrations) and achieving a steady angular velocity as quickly as possible (over an angle of 28°). The voltage across the tachometer was sampled together with the force signals (see below) at 50 Hz. Angular velocity during the experiments was determined from the tachometer signal, so any small deviations in motor speed (e.g. due to higher torques at higher angles of attack) were accounted for.

The mean Reynolds number (Re) for a flapping wing is a somewhat arbitrary definition (e.g. Ellington, 1984f; Van den Berg and Ellington, 1997a), but it appears unlikely that the hovering hawkmoths of Willmott and Ellington (1997a–c) were operating anywhere near a critical value: both larger and smaller insects can hover in a fundamentally similar way; wing stroke amplitude, angle of attack and stroke plane are consistent for the wide range of insects that undertake 'normal hovering' (Weis-Fogh, 1973; Ellington, 1984c). Because of

this, and the benefits in accuracy when using larger forces, a fairly high rotational frequency (0.192 Hz) was chosen. Following the conventions of Ellington (1984f), this produces an Re of 8071. While this is a little higher than that derived from the data of Willmott and Ellington (1997b) for F1 (Re=7300), the hawkmoth selected below for a 'standard' wing design, it is certainly within the range of hovering hawkmoths.

Wing design

The wings were constructed from 500 mm×500 mm× 2.75 mm sheets of black plastic 'Fly-weight' envelope stiffener. This material consists of two parallel, square, flat sheets sandwiching thin perpendicular lamellae that run between the sheets for the entire length of the square. The orientation of these lamellae results in hollow tubes of square cross section running between the upper and lower sheets from leading to trailing edge. Together, this structure and material produces relatively stiff, light, thin, strong wing models.

The standard hawkmoth wing planform was derived from a female hawkmoth 'F1' described by Willmott and Ellington (1997a,b) (Fig. 2A). F1 was selected as the most representative because its aspect ratio and radii for moments of area were closest to the average values found from previous studies (Ellington, 1984b; Willmott and Ellington, 1997b). The wing was connected to the sting on the propeller head by a 2.4 mm diameter steel rod running down a 20 mm groove cut in the ventral surface of the wing. The groove was covered in tape, resulting in an almost flat surface barely protruding from the wing material. The rod also defined the angle of attack of the wing as it was gripped by grub-screws at the sting and bent at right angles within the wing to run internally down one of the 'tubes' formed by the lamellae. A representative zero geometric angle of attack α was set by ensuring that the base chord of each wing was horizontal. The rotation of each sting (about the pronation/supination axis) could be set independently in increments of 5° using a 72-tooth cog-and-pallet arrangement. The leading and trailing edges of the wings were taped, producing bluff edges less than 3 mm thick. The wing thickness was less than 1.6% of the mean chord.

Leading-edge range

Three variations on the standard, flat, hawkmoth wing model were constructed. 'Sharp' leading edges were produced by sticking a 10 mm border of 0.13 mm brass shim to the upper surface of the leading edge of standard hawkmoth wing models which had had 10 mm taken off the leading edges. The converse of this, wings with 'thick' leading edges, was achieved by using two layers of the plastic wing material, resulting in wings of double thickness. While this confounds leading-edge thickness and wing thickness, it allowed wings to be produced that had thick leading edges without also distinct steps in the upper or lower surface. The third design was of standard thickness and had a 'sawtooth' leading edge of 45° pitch (Fig. 2B), with sawteeth 10 mm deep and 10 mm long.
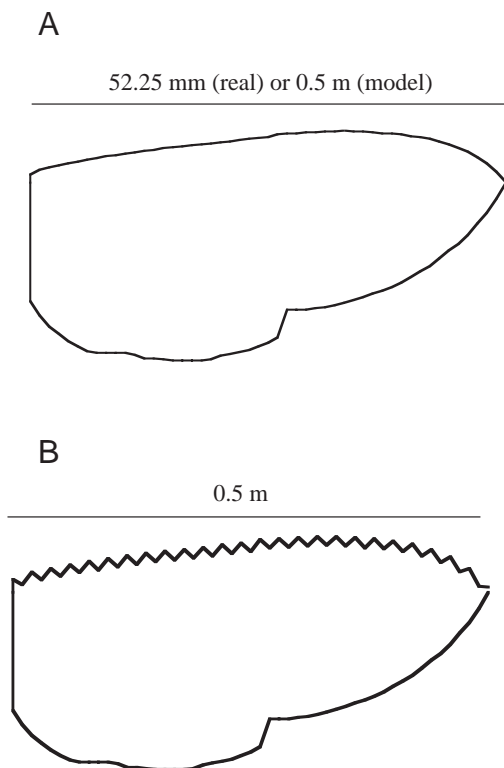
A

52.25 mm (real) or 0.5 m (model)

B

0.5 m

Fig. 2. Standard (A) and 'sawtooth' (B) hawkmoth planforms.

Twist range

Twisted wing designs were produced by introducing a second 2.4 mm diameter steel rod, which ran down the central groove, with bends at each end running perpendicularly down internal tubes at the wing base and near the tip. The two ends of the rod were out of plane, thus twisting the wing, creating a lower angle of attack at the wing tip than at the base. One wing pair had a twist of 15° between base and tip, while the second pair had a twist of 32°. No measurable camber was given to the twisted wings.

The wing material was weakened about the longitudinal axis of the wing by alternately slicing dorsal and ventral surfaces, which destroyed the torsion box construction of the internal 'tubes'. This slicing was necessary to accommodate the considerable shear experienced at the trailing and leading edges, far from the twist axis.

Camber range

Standard hawkmoth wing models were heat-moulded to apply a camber. The wings were strapped to evenly curved steel sheet templates and placed in an oven at 100°C for approximately 1 h. The wings were then allowed to cool overnight. The wings 'uncambered' to a certain extent on removal from the templates, but the radius of curvature remained fairly constant along the span, and the reported cambers for the wings were measured *in situ* on the propeller. For thin wings, camber can be described as the ratio of wing depth to chord. One wing pair had a 7 % camber over the basal half of the wing: cambers were smaller at the tip because of the narrower chord. The second wing pair had a 10 % camber over the same region. The application of camber also gave a small twist of less that 6° to the four wing models.

Wing moments

The standard wing shape used was a direct copy of the hawkmoth F1 planform except in the case of the sawtooth leading-edge design. However, the model wings do not revolve exactly about their bases: the attachment 'sting' and propeller head displace each base by 53.5 mm from the propeller axis. Since the aerodynamic forces are influenced by both the wing area and its distribution along the span, this offset must be taken into account.

Table 1 shows the relevant wing parameters for aerodynamic analyses, following Ellington's (1984b) conventions. The total wing area S (for two wings) can be related to the single wing length R and the aspect ratio AR:

$$S = 4R^2/AR. \tag{1}$$

Aerodynamic forces and torques are proportional to the second and third moments of wing area, S_2 and S_3 respectively (Weis-Fogh, 1973). Non-dimensional radii, $\hat{r}_2(S)$ and $\hat{r}_3(S)$, corresponding to these moments are given by:

$$\hat{r}_2(S) = (S_2/SR^2)^{1/2} \tag{2}$$

and

$$\hat{r}_3(S) = (S_3/SR^3)^{1/3}. \tag{3}$$

Table 1. *Wing parameters for real and model hawkmoth wings*

	Hawkmoth F1	Model hawkmoth wing with offset	Model sawtooth hawkmoth wing with offset
R (mm)	52.25	556	556
AR	5.66	6.34	6.33
$\hat{r}_2(S)$	0.511	0.547	0.547
$\hat{r}_3(S)$	0.560	0.588	0.588

R, wing length; AR, aspect ratio; $\hat{r}_2(S)$, $\hat{r}_3(S)$, non-dimensional second and third moments of area.

Non-dimensional values are useful as they allow differences in wing shape to be identified while controlling for wing size.

The accuracy of the wing-making and derivation of moments was checked after the experiments by photographing and analysing the standard 'flat' hawkmoth wing. Differences between the expected values of S_2 and S_3 for the model wings and those observed after production were less than 1 %.

Smoke observations

Smoke visualisation was performed independently from force measurements. Vaporised Ondina EL oil (Shell, UK) from a laboratory-built smoke generator was fed into a chamber of the propeller body and from there into the hollow shaft. This provided a supply of smoke at the propeller head, even during continuous revolution. Smoke was then delivered from the propeller head to the groove in the ventral surface of the wing by 4.25 mm diameter Portex tubing. A slight pressure from the smoke generator forced smoke to disperse down the groove, down the internal wing 'tubes' and out of the leading and trailing edges of the wing wherever the tape had been removed. Observations were made directly or *via* a video camera mounted directly above the propeller. Photographs were taken using a Nikon DS-560 digital camera with 50 mm lens. Lighting was provided by 1 kW Arri and 2.5 kW Castor spotlights. A range of rotational speeds was used: the basic flow properties were the same for all speeds, but a compromise speed was necessary. At high speeds, the smoke spread too thinly to photograph, while at low speeds the smoke jetted clear of the boundary layer and so failed to label any vortices near the wing. A wing rotation frequency of 0.1 Hz was used for the photographs presented here.

Force measurements

Measurement of vertical force

The propeller body was clamped to a steel beam by a brass sleeve. The beam projected horizontally, perpendicular to the propeller axis, over a steel base-plate (Fig. 1B). The beam (1.4 m long, 105 mm deep and 5 mm wide) rested on a knife-blade fulcrum, which sat in a grooved steel block mounted on the base-plate. Fine adjustment of the balance using a counterweight allowed the beam to rest gently on a steel shim cantilever with foil strain gauges mounted on the upper and lower surfaces. The shim was taped firmly to the beam and

deflected in response to vertical forces acting on the propeller on the other side of the fulcrum because of the 'see-saw' configuration. The strain gauges were protected from excessive deflection by a mechanical stop at the end of the beam. Signals from these 'vertical force' strain gauges were amplified and fed into a Macintosh Quadra 650 using LabVIEW to sample at 50 Hz. The signal was calibrated using a 5 g mass placed at the base of the propeller, directly in line with the propeller axis. No hysteresis between application and removal of the mass was observed, and five calibration measurements were made before and after each experiment. The mean coefficient of variation for each group of five measurements was less than 2 %, and there was never a significant change between calibrations before and after each experiment.

The upper edge of the steel beam was sharpened underneath the area swept by the propeller wings to minimise aerodynamic interference. The beam was also stiffened by a diamond structure of cables, separated by a 10 mm diameter aluminium tube sited directly over the fulcrum.

Measurement of torque

The torque Q required to drive the wings was measured *via* a pair of strain gauges mounted on a shim connected to the axle of the propeller (Fig. 1, iv). The signal from these strain gauges was pre-amplified with revolving electronics, also attached to the shaft, before passing through electrical slip-rings (through which the power supply also passed) machined from circuit board. The signal was then amplified again before being passed to the computer, as with the vertical force signal.

The torque signal was calibrated by applying a known torque: a 5 g mass hung freely from a fine cotton thread, which passed over a pulley and wrapped around the propeller head. This produced a 49.1 mN force at a distance of 44 mm from the centre of the axle and resulted in a calibration torque of 2.16 mN m. This procedure was extremely repeatable and showed no significant differences throughout the experiments. Five calibration readings were recorded before and after each experiment. The mean coefficient of variation for each group of five measurements was less than 6 %.

Torques due to friction in the bearings above the strain gauges and to aerodynamic drag other than that caused by the wings were measured by running the propeller without wings. This torque was subtracted from the measurements with wings, giving the torque due to the wing drag only. It is likely, however, that this assessment of non-aerodynamic torque is near the limit of the force transducers, and is somewhat inaccurate, because the aerodynamic drag measured for wings at zero angle of incidence was apparently slightly less than zero.

Experimental protocol

Each wing type was tested twice for a full range of angles of attack from –20 to +95 ° with 5 ° increments and three times using an abbreviated test, covering from –20° to +100° in 20° increments. Four runs were recorded at each angle of attack, consisting of approximately 10 s before the motor was turned
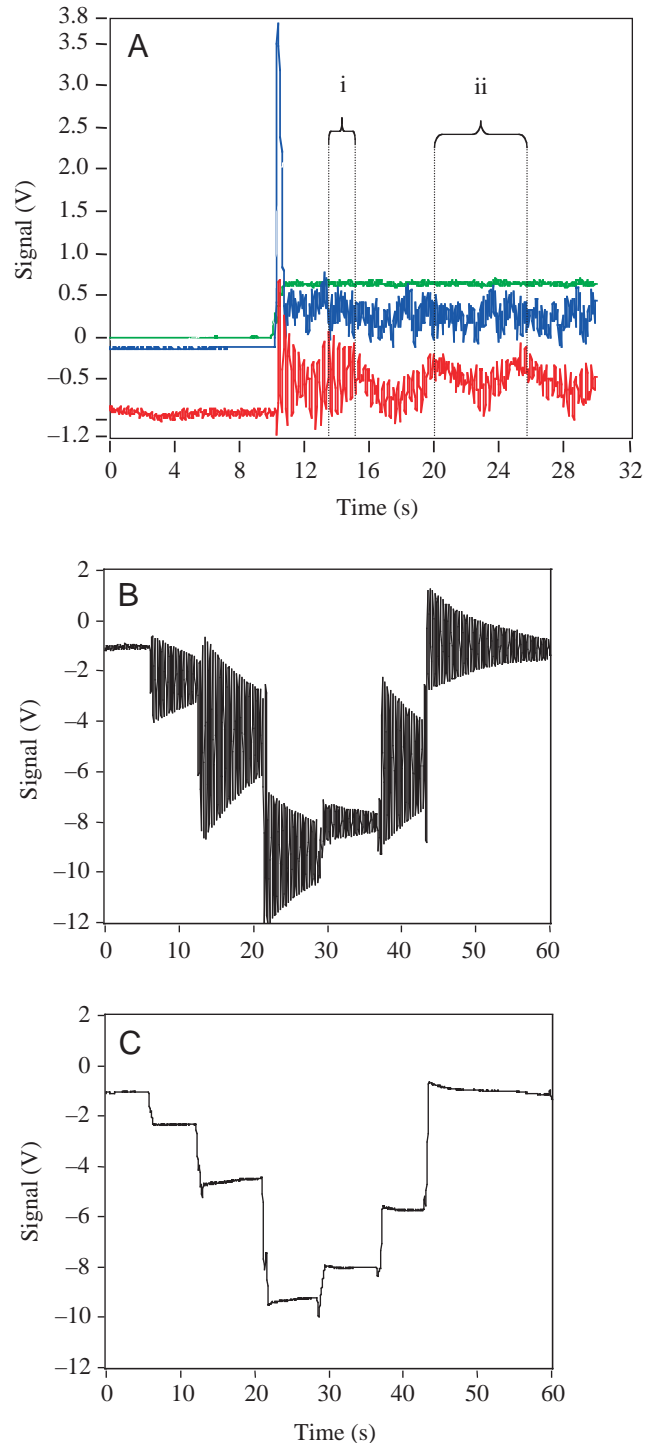

Fig. 3. Typical voltage signals for a single run at high angle of attack α (A) and response of the vertical force transducer to the addition, and then removal, of 5, 10 and 20 g before (B) and after (C) filtering. In A, the top (green) line shows the tachometer trace, the middle (blue) line the torque signal and the bottom (red) line the vertical force signal. The wings were started after 10 s. Vertical dotted lines identify five oscillations due to the lightly damped 'mass-spring' system (i) inherent in the vertical transducer design, and one cycle due to a mass imbalance of the wings (ii) during a complete revolution.

on followed by 20 s after the propeller had started. The starting head positions for these four runs were incremented by 90°, and pairs of runs started at opposite positions were averaged to cancel any imbalance in the wings. Overall, –20, 0, 20, 40, 60 and 80° had 10 independent samples each, 100° had six, and all the other angles of attack had four.

Data processing

Once collected, the data were transferred to a 400 MHz Pentium II PC and analysed in LabVIEW. Fig. 3A shows a typical trace for a single run. The top (green) trace shows the tachometer signal, with the wing stationary for the first 10 s. The middle (blue) trace shows the torque signal: a very large transient is produced as the torque overcomes the inertia of the wings, and the signal then settles down. The bottom (red) trace shows the vertical force signal.

The rise in the tachometer signal was used to identify the start of wing movement. Zero values for the force signals were defined as the means before the wings started moving; from then on, signal values were taken relative to their zero values.

Filtering

Force and torque signals were low-pass-filtered at 6 Hz using a finite impulse response filter. Large-amplitude oscillations persisted in the vertical force signal. These are due to the massive propeller and beam resting on the vertical force strain gauge shim, thus producing a lightly damped mass-spring system. A simple physical argument allows this oscillation to be removed effectively. A moving average, taken over the period of oscillation, consists only of the aerodynamic force and the damping force: mean inertial and spring forces are zero over a cycle. When the damping force is negligible, this method will yield the mean aerodynamic force with a temporal resolution of the order of the oscillation period. This simple 'boxcar' filtering technique was tested on a signal created by the addition and removal of a range of masses to the propeller head (Fig. 3B). The removal of the oscillation from the signal was highly effective (Fig. 3C), and the full change in signal was observed after a single oscillation period (0.32 s) had passed. This 'step' change corresponded to the static calibration of the vertical strain gauge, confirming that the damping force was indeed negligible. The longer-period oscillation visible in the vertical force signal trace (Fig. 3A) is due to a slight difference in mass between the wings. The effect of this imbalance is cancelled by averaging runs started in opposite positions.

A similar filtering technique was used on the torque signal. Unlike the vertical force signal,

however, several modes of vibration were observed. A large filter window size (1.28 s) was needed to remove the dominant mode, but resulted in a poorer temporal resolution (equivalent to approximately a quarter-revolution).

Pooling the data into 'early' and 'steady' classes

The filtered data for each angle of attack was pooled into 'early' or 'steady' classes. 'Early' results were averaged force coefficients relating to the first half-revolution of the propeller, between 60 and 120° from the start of revolution, 1.5–3.1 chord-lengths of travel of the middle of the wing. This excluded the initial transients and ensured that the large filter window for the torque signal did not include any data beyond 180°. *A priori* assumptions were not made about the time course for development of the propeller wake, so force results from between 180 and 450° from the start of revolution were averaged and form the 'steady' class. The large angle over which 'steady' results were averaged and the relative constancy of the signal for many revolutions (Fig. 4) suggest
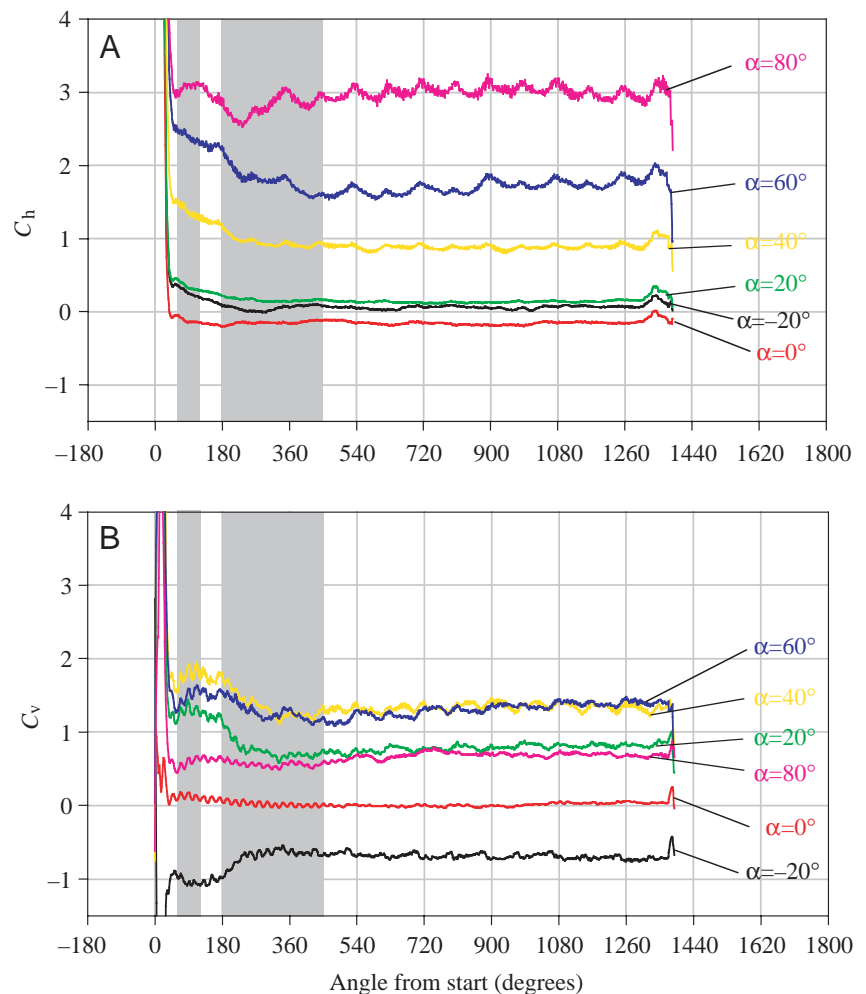

Fig. 4. Averaged horizontal C_h (A) and vertical C_v (B) force coefficients plotted against angle of revolution for standard hawkmoth wings over the 'abbreviated' range of angle of attack α. Underlying grey panels show the averaging period for 'early' (narrower panel) and 'steady' (broader) pools.

that the 'steady' results are close to those that would be found for propellers that have achieved steady-state revolution, with a fully developed wake. However, it should be noted that brief high (or low), dynamic and biologically significant forces, particularly during very early stages of revolution, are not identifiable with the 'early' pooling technique.

Coefficients

Conversion into 'propeller coefficients'

Calibrations before and after each experiment were pooled and used to convert the respective voltages to vertical forces (N) and torques (N m). 'Propeller coefficients' analogous to the familiar lift and drag coefficients will be used for a dimensionless expression of vertical and horizontal forces F_v and F_h, respectively: lift and drag coefficients are not used directly because they must be related to the direction of the oncoming air (see below).

The vertical force on an object, equivalent to lift if the incident air is stationary is given by:

$$F_v = \frac{\rho}{2} C_v S V^2 , \qquad (4)$$

where ρ is the density of air (taken to be $1.2\,\text{kg m}^{-3}$), C_v is the vertical force coefficient, S is the area of both wings and V is the velocity of the object. A pair of revolving wings may be considered as consisting of many objects, or 'elements'. Each element, at a position r from the wing base, with width dr and chord c_r, has an area $c_r dr$ and a velocity U given by:

$$U = \Omega r , \qquad (5)$$

where Ω is the angular velocity (in rad s^{-1}) of the revolving wings.

The 'mean coefficients' method of blade-element analysis (first applied to flapping flight by Osborne, 1951) supposes that a single mean coefficient can represent the forces on revolving and flapping wings. So, the form of equation 4 appropriate for revolving wings is:

$$F_v = 2 \frac{\rho}{2} C_v \sum_{r=0}^{r=R} c_r dr (\Omega r)^2 . \qquad (6)$$

The initial factor of 2 is to account for both wings. Ω is a constant for each wing element, and so equation can be written:

$$F_v = \frac{\rho}{2} \Omega^2 C_v \left(2 \sum_{r=0}^{r=R} c_r r^2 dr \right) . \qquad (7)$$

The term in parentheses is a purely morphological parameter, the second moment of area S_2 of both wings (see Ellington, 1984b). From these expressions, the mean vertical force coefficient C_v can be derived:

$$C_v = \frac{2 F_v}{\rho S_2 \Omega^2} . \qquad (8)$$

The mean horizontal force coefficient C_h can be determined in a similar manner. The horizontal forces (equivalent to drag if

the relative air motion is horizontal) for each wing element act about a moment arm of length r measured from the wing base and combine to produce a torque Q. Thus, the equivalent of equation 7 uses a cubed term for r:

$$Q = \frac{\rho}{2} \Omega^2 C_h \left(2 \sum_{r=0}^{r=R} c_r r^3 dr \right) . \qquad (9)$$

In this case the term in parentheses is the third moment of wing area S_3 for both wings. The mean horizontal force coefficient C_h is given by:

$$C_h = \frac{2Q}{\rho S_3 \Omega^2} . \qquad (10)$$

Coefficients derived from these propeller experiments, in which the wings revolve instead of translate in the usual rectilinear motion, are termed 'propeller coefficients'.

Conversion into conventional profile drag and lift coefficients

If the motion of air about the propeller wings can be calculated, then the steady propeller coefficients can be converted into conventional coefficients for profile drag $C_{D,pro}$ and lift C_L. The propeller coefficients for 'early' conditions provide a useful comparison for the results of these conversions; the induced downwash of the propeller wake has hardly begun, so $C_{D,pro}$ and C_L approximate $C_{h,early}$ and $C_{v,early}$. However, wings in 'early' revolution do not experience completely still air; some downwash is produced even without the vorticity of the fully developed wake. Despite this, $C_{h,early}$ and $C_{v,early}$ provide the best direct (though under-) estimates of $C_{D,pro}$ and lift C_L for wings in revolution.

Consider the wing-element shown in Fig. 5, which shows the forces (where the prime denotes forces per unit span) acting on a wing element in the two frames of reference. A downwash
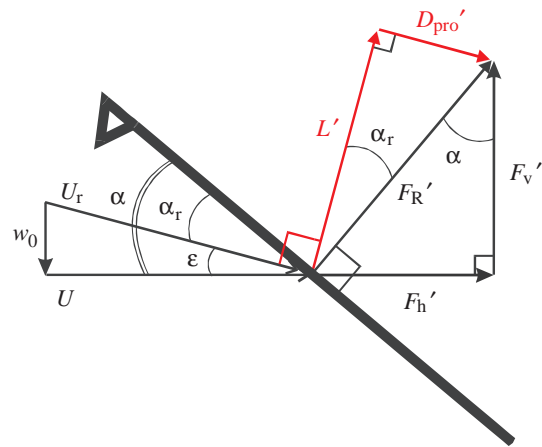

Fig. 5. Flow and force vectors relating to a wing element. U, velocity of wing element; U_r, relative velocity of air at a wing element; w_0, vertical component of induced downwash velocity; α, geometric angle of attack; α_r, effective angle of attack; ε, downwash angle; F_h' and F_v', orthogonal horizontal and vertical forces; F_R', single resultant force; L' and D_{pro}', orthogonal lift and profile drag forces.

air velocity results in a rotation of the 'lift/profile drag' from the 'vertical/horizontal' frame of reference by the downwash angle ε. In the 'lift/profile drag' frame of reference, a component of profile drag acts downwards. Also, a component of lift acts against the direction of motion; this is conventionally termed 'induced drag'. A second aspect of the downwash is that it alters the appropriate velocities for determining coefficients; C_h and C_v relate to the wing speed U, whereas $C_{D,pro}$ and C_L relate to the local air speed U_r.

If a 'triangular' downwash distribution is assumed, with local vertical downwash velocity w_0 proportional to spanwise position along the wing r (which is reasonable, and the analysis is not very sensitive to the exact distribution of downwash velocity; see Stepniewski and Keys, 1984), then there is a constant downwash angle ε for every wing chord. Analysis of induced downwash velocities by conservation of momentum, following the 'Rankine–Froude' approach, results in a mean vertical downwash velocity $\overline{w_0}$ given by:

$$\overline{w_0} = k_{ind} \sqrt{\frac{F_v}{2\rho\pi R^2}} \,, \qquad (11)$$

where k_{ind} is a correction factor accounting for non-uniform (both spatially and temporally) downwash distributions. $k_{ind}=1.2$ is used in this study (following Ellington, 1984e) but, again, the exact value is not critical. The local induced downwash velocity, given the triangular downwash distribution and maintaining the conservation of momentum, is given by (Stepniewski and Keys, 1984):

$$w_0 = \frac{\overline{w_0}r\sqrt{2}}{R} \,, \qquad (12)$$

and so the value of w_0 appropriate for the wing tip is $\overline{w_0}\sqrt{2}$. Given that the wing velocity at the tip is ΩR, the downwash angle ε is given by:

$$\varepsilon = \tan^{-1}\left(\frac{\overline{w_0}\sqrt{2}}{\Omega R}\right). \qquad (13)$$

If small angles are assumed, then the approximations

$$C_{D,pro} \approx C_h\cos\varepsilon \qquad (14)$$

and

$$C_L \approx C_v\cos\varepsilon \qquad (15)$$

may be used. However, these approximations can be avoided: it is clear from Fig. 5 that the forces can be related by:

$$F_h' = L'\sin\varepsilon + D_{pro}'\cos\varepsilon \qquad (16)$$

and

$$F_v' = L'\cos\varepsilon - D_{pro}'\sin\varepsilon . \qquad (17)$$

From these:

$$D_{pro}' = F_h'\cos\varepsilon - F_v'\sin\varepsilon \qquad (18)$$

and

$$L' = F_v'\cos\varepsilon + F_h'\sin\varepsilon . \qquad (19)$$

The appropriate air velocities for profile drag and lift coefficients may be described conveniently as proportions of the wing velocity. In simple propeller theories, a vertical downwash is assumed, and the local air velocity U_r at each element, as a proportion of the velocity of the wing element U, is given by:

$$\frac{U_r}{U} = \frac{1}{\cos\varepsilon} \,. \qquad (20)$$

More sophisticated propeller theories postulate that the induced velocity is perpendicular to the relative air velocity U_r because that is the direction of the lift force and, hence, the direction of momentum given to the air. A 'swirl' is therefore imparted to the wake by the horizontal component of the inclined induced velocity. Estimating the induced velocity, ε and U_r, then becomes an iterative process because they are all coupled, but for small values of ε we can use the approximate relationship:

$$\frac{U_r}{U} \approx \cos\varepsilon \,, \qquad (21)$$

i.e. the relative velocity is slightly smaller than U, whereas the assumption of a vertical downwash makes it larger than U. Thus, the ratio of wing-element velocity to local air velocity may be estimated from the downwash angle, ε, in two ways, given by equations 11 and 13.

Given the rotation of the frames of reference described in equations 18 and 19, and the change in relevant velocities discussed for equations 20 and 21, profile drag and lift coefficients can be derived from 'steady' propeller coefficients:

$$C_{D,pro} = (C_{h,steady}\cos\varepsilon - C_{v,steady}\sin\varepsilon)\left(\frac{U}{U_r}\right)^2 \qquad (22)$$

and

$$C_L = (C_{v,steady}\cos\varepsilon + C_{h,steady}\sin\varepsilon)\left(\frac{U}{U_r}\right)^2. \qquad (23)$$

Display of results

Angle of incidence

The definition of a single geometric angle of attack α is clearly arbitrary for cambered and twisted wings, so angles were determined with respect to a zero-lift angle of attack α_0. This was found from the x-intercept of a regression of 'early' C_v data ($C_{v,early}$) against a range of α from $-20\,°$ to $+20\,°$. The resulting angles of incidence, $\alpha'=\alpha-\alpha_0$, were thus not pre-determined; the experimental values were not the same for each wing type, although the increment between each α' within a wing type is still $5\,°$. The use of angle of incidence allows comparison between different wing shapes without any bias introduced by an arbitrary definition of geometric angle of attack.

Determination of significance of differences

Because the zero-lift angle differs slightly for each wing type, the types cannot be compared directly at a constant angle of incidence. Instead, it is useful to plot the relationships

between force coefficients and angles with a line width of ± one mean standard error (S.E.M.): this allows plots to be distinguished and, at these sample sizes (and assuming parametric conditions are approached), the lines may be considered significantly different if (approximately) a double line thickness would not cause overlap between lines. The problems of sampling in statistics should be remembered, so occasional deviations greater than this would be expected without any underlying aerodynamic cause.

Results
Force results
Typical changes of force coefficient with angle of revolution

Fig. 4 shows variations in propeller coefficients with the angle of revolution for standard 'flat' hawkmoth wings over the 'abbreviated' range of angles. Each line is the average of six independent samples at the appropriate α.

Standard hawkmoth

Fig. 6 shows C_h and C_v plotted against α' for the standard flat hawkmoth model wing pair. The minimum C_h is not significantly different from zero and is, in fact, slightly negative. This illustrates limits to the accuracy of the measurements. Significant differences are clear between 'early' and 'steady' values for both vertical and horizontal coefficients over the mid-range of angles. Maximal values of C_h occur at α' around 90°, and C_v peaks between 40 and 50°. The error bars shown (± 1 S.E.M.) are representative for all wing types.

In Figs 7–9, standard hawkmoth results are included as an underlying grey line and represent 0° twist and 0% camber.

Leading-edge range

Fig. 7 shows C_h and C_v plotted against α' for hawkmoth wing models with a range of leading-edge forms. The relationships between force coefficients and α' are strikingly similar, especially for the 'steady' values (as might be expected from the greater averaging period). The scatter visible in the polar diagram (Fig. 7C) incorporates errors in both C_h and C_v, making the scatter more apparent than in Fig. 7A,B.

Twist range

Fig. 8 shows C_h and C_v plotted against α' for twisted hawkmoth wing models. Results for the 15° twist are not significantly different from those for the standard flat model. For the 32° twist, however, C_h and C_v plotted against α' both decrease under 'early' and 'steady' conditions at moderate to large angles of incidence. This is emphasised in the polar diagram (Fig. 8C), which shows that the maximum force coefficients for the 32° twist are lower than for the less twisted wings. The degree of shift between 'early' and 'steady' force coefficients is not influenced by twist.

Camber range

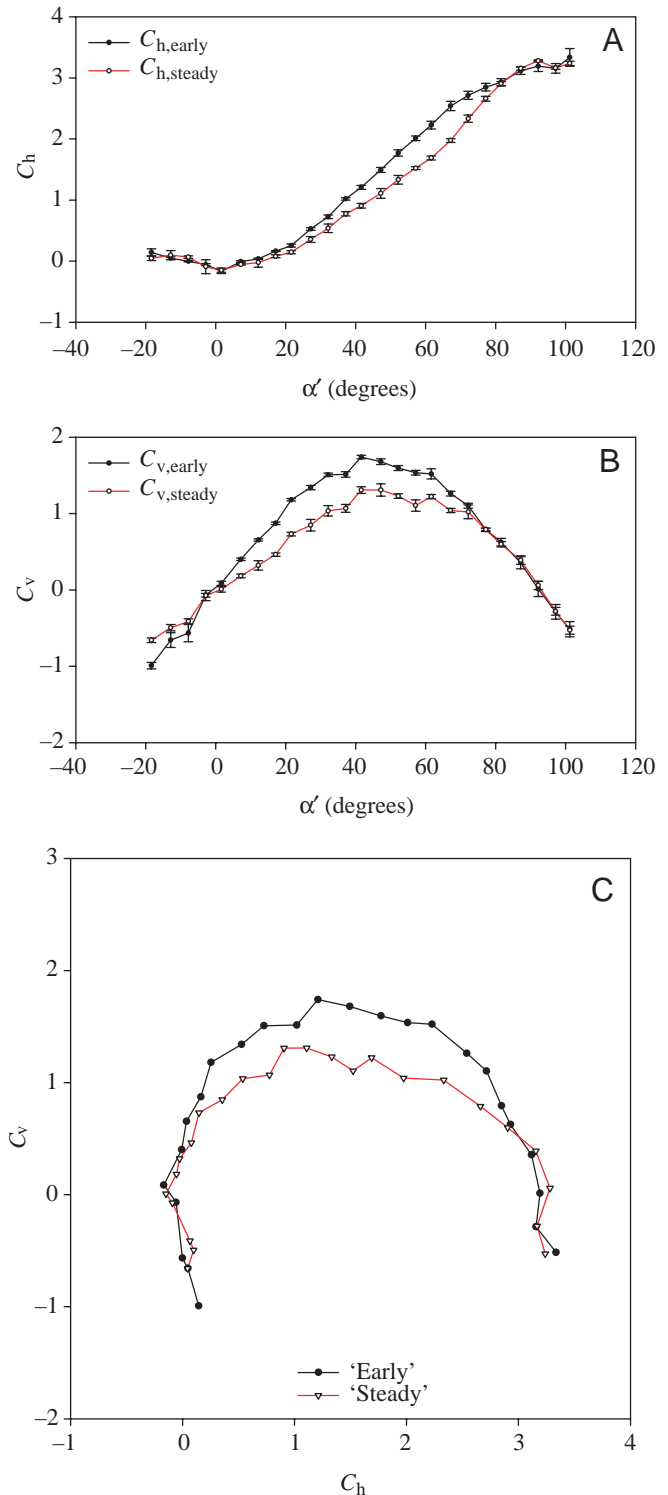Fig. 9 shows C_h and C_v plotted against α' for cambered

Fig. 6. Horizontal C_h (A) and vertical C_v (B) force coefficients and the polar diagram (C) for standard hawkmoth wings under 'early' and 'steady' conditions. Error bars in A and B show ±1 S.E.M., N=4–10. α', angle of incidence.

hawkmoth wing models, and the corresponding polar diagrams are presented in Fig. 9C. Consistent differences, if present, are very slight.
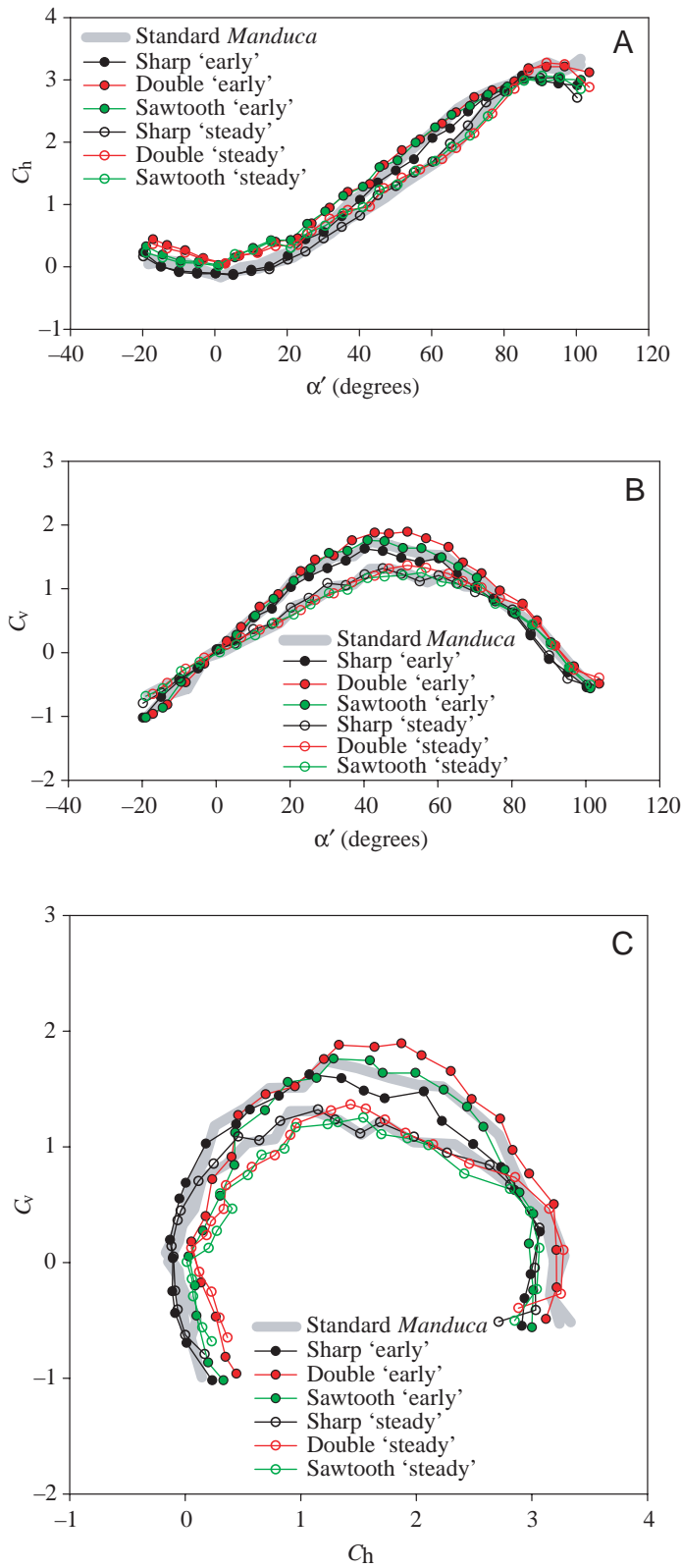
Fig. 7. Horizontal C_h (A) and vertical C_v (B) force coefficients and the polar diagram (C) for the 'leading-edge' range under 'early' and 'steady' conditions. Underlying grey lines show 'early' (higher) and 'steady' (lower) values for standard hawkmoth wings and represent 0° twist and 0% camber. α', angle of incidence.
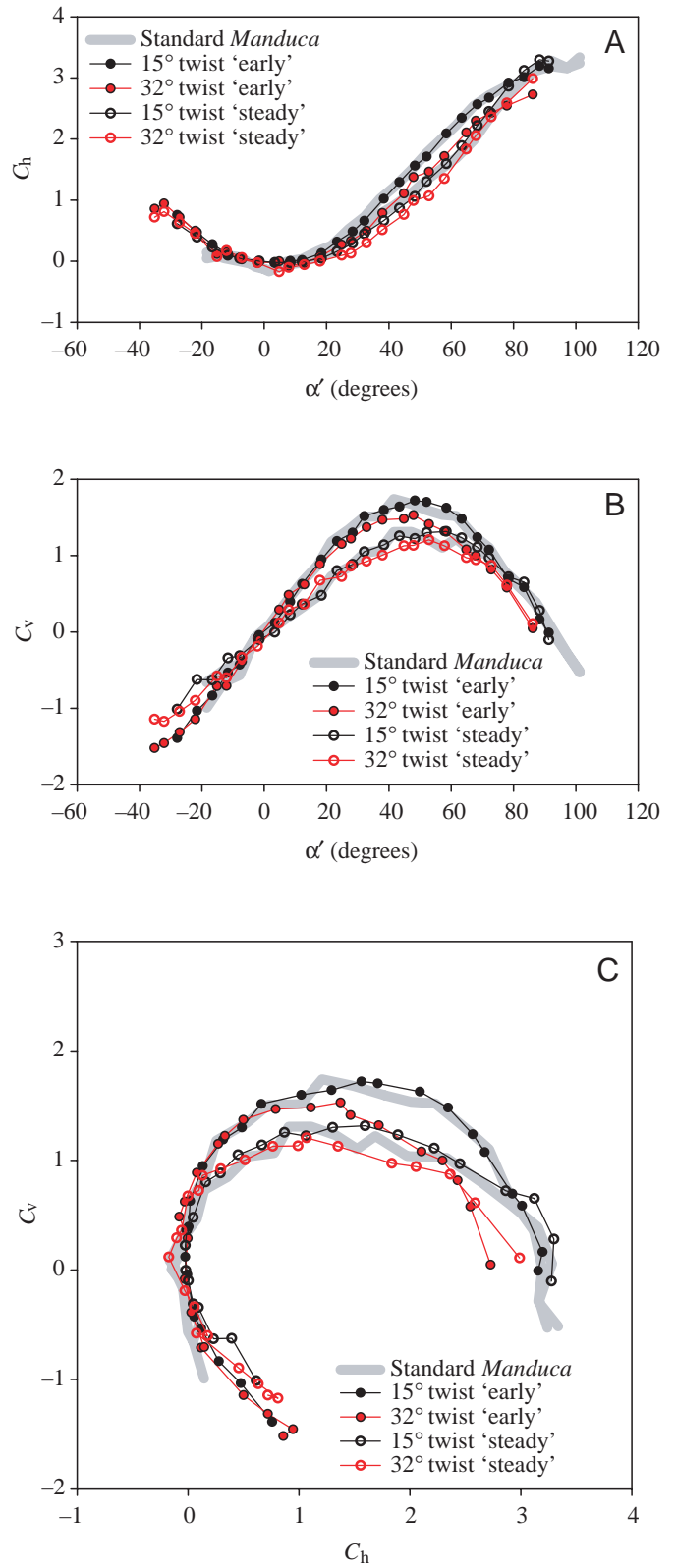
Fig. 8. Horizontal C_h (A) and vertical C_v (B) force coefficients and the polar diagram (C) for hawkmoth wings with a range of twist under 'early' and 'steady' conditions. Underlying grey lines show 'early' (higher) and 'steady' (lower) values for standard hawkmoth wings. α', angle of incidence.
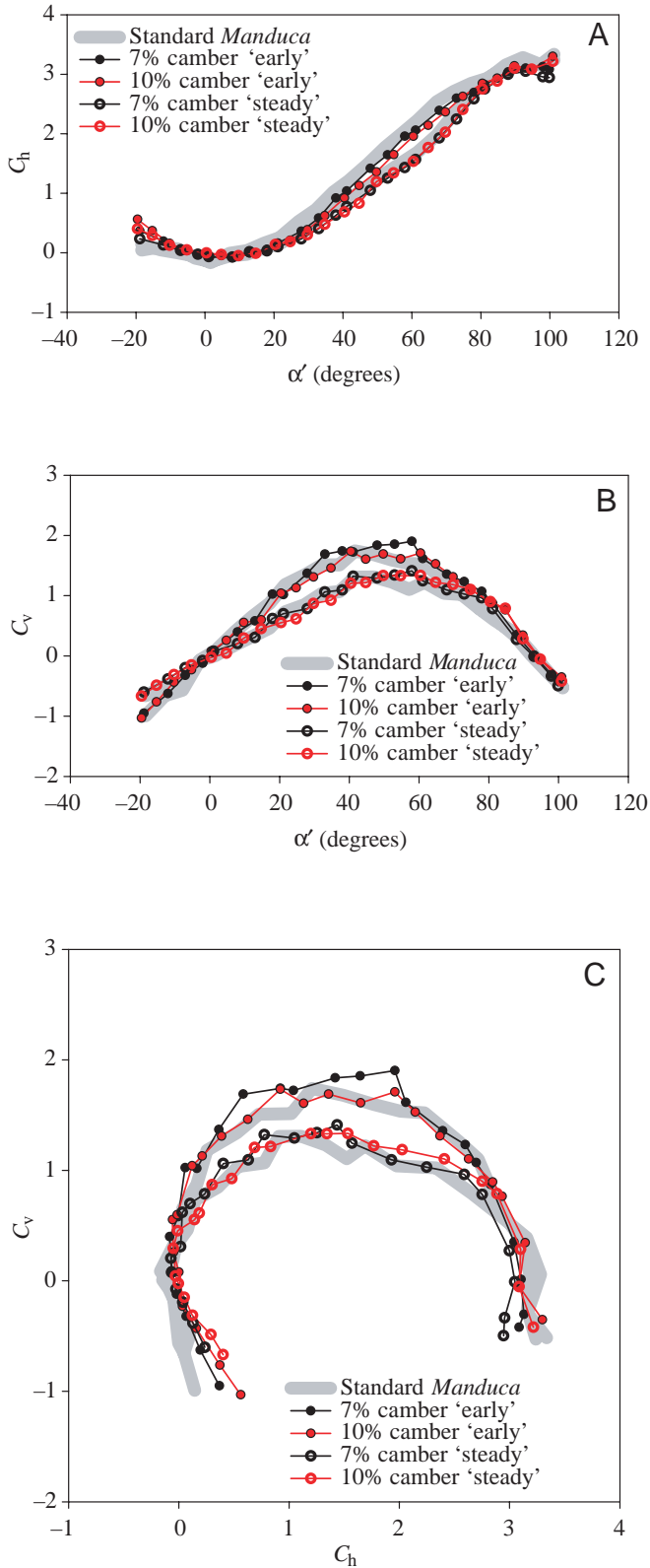
Fig. 9. Horizontal C_h (A) and vertical C_v (B) force coefficients and the polar diagram (C) for hawkmoth wings with a range of camber under 'early' and 'steady' conditions. Underlying grey lines show 'early' (higher) and 'steady' (lower) values for standard hawkmoth wings. α′, angle of incidence.

Conversion into profile drag and lift coefficients

Fig. 10 shows the results of the three methods for estimating $C_{D,pro}$ and C_L derived above, based on the mean values for all wings in the 'leading-edge' range. The 'small-angle' model uses equations 14 and 15; the 'no-swirl' model uses the large-angle equations 18 and 19 and the assumption that the downwash is vertical (equation 20); the 'with-swirl' model uses the large-angle expressions and the assumption that the induced velocity is inclined to the vertical (equation 21).

The 'small-angle' model is inadequate; calculated profile drag and lift coefficients are very close to 'steady' propeller coefficients and do not account for the shift in forces between 'early' and 'steady' conditions. Both models using the large-angle expressions provide reasonable values of $C_{D,pro}$ and C_L for α′ up to 50°; agreement with the 'early' propeller coefficient polar is very good. Above 50°, both models, especially the 'no-swirl' model, appear to underestimate C_L.

Air-flow observations

Smoke emitted from the leading and trailing edges and from holes drilled in the upper wing surface labels the boundary layer over the wing (Fig. 11). At very low angles of incidence (Fig. 11A), the smoke describes an approximately circular path about the centre of revolution, with no evidence of separation or spanwise flow. Occasionally at small angles of incidence (e.g. 10°), and consistently at all higher angles of incidence, smoke separates from the leading edge and travels rapidly towards the tip ('spanwise' or 'radially'). The wrapping up of this radially flowing smoke into a well-defined spiral 'leading-edge vortex' is visible under steady revolution (Fig. 11B) and starts as soon as the wings start revolving.

Near the wing tip, the smoke labels a large, fairly dispersed tip- and trailing-vortex structure. At extreme angles of incidence (including 90°), flow separates at the trailing edge in a similar manner to separation at the leading edge (the Kutta condition is not maintained): stable leading- and trailing-edge vortices are maintained behind the revolving wing, and both exhibit a strong spanwise flow.

The smoke flow over the 'sawtooth' design gave very similar results.

Discussion

Three points are immediately apparent from the results presented above. First, both vertical and horizontal force coefficients are remarkably large. Second, even quite radical changes in wing form have relatively slight effects on aerodynamic properties. In the subsequent discussion, 'pooled' values refer to the averaged results from all flat (uncambered, untwisted) wings for the whole 'leading-edge range'. Pooling reduces noise and can be justified because no significant differences in aerodynamic properties were observed over the range. Third, a significant shift in coefficients is visible between 'early' and 'steady' conditions.

Vertical force coefficients are large

If 'early' values for C_v provide minimum estimates for 'propeller' lift coefficients (since the propeller wake, and thus also the downwash, is not fully developed), then the maximum lift coefficient $C_{L,max}$ for the 'pooled' data is 1.75, found at $\alpha'=41°$. Willmott and Ellington (1997c) provide steady-state force coefficients for real hawkmoth wings in steady, translational flow over a range of Re. Their results for $Re=5560$ are shown with the 'pooled' data for flat wings in Fig. 12. The differences are remarkable: the revolving model wings produce much higher force coefficients. The maximum vertical force coefficient for the real wings in translational flow, 0.71, is considerably less than the 1.5–1.8 required to support the weight during hovering. Willmott and Ellington (1997c) therefore concluded that unsteady aerodynamic mechanisms must operate during hovering and slow flight. The same conclusions have previously been reached for a variety of animals for which the values of C_L required for weight support are well above 1.5 and sometimes greater than 2.

The result presented in this study, that high force coefficients can be found in steadily revolving wings, suggests that the importance of unsteady mechanisms, increasingly assumed since Cloupeau et al. (1979) (Ennos, 1989; Dudley and Ellington, 1990b; Dudley, 1991; Dickinson and Götz, 1993; Wells, 1993; Wakeling and Ellington, 1997b; Willmott and Ellington, 1997c), particularly after the work of Ellington (1984a–f), may need some qualification. It should instead be concluded that unsteady *and/or* three-dimensional aerodynamic mechanisms normally absent for wings in steady, translational flow are needed to account for the high lift coefficients in slow flapping flight.

Most wind-tunnel experiments on wings confound the two factors: flow is steady, and the air velocity at the wing base is the same as that at the wing tip. Such experiments have resulted in maximum lift coefficients of around or below 1: dragonflies of a range of species reach 0.93–1.15 (Newman et al., 1977; Okamoto et al., 1996; Wakeling and Ellington, 1997b), the cranefly *Tipula oleracea* achieves 0.86 (Nachtigall, 1977), the fruitfly *Drosophila virilis* 0.87 (Vogel, 1967b) and the bumblebee *Bombus terrestris* 0.69 (Dudley and Ellington, 1990b). Jensen (1956), however, created an appropriate spanwise velocity gradient by placing a smooth, flat plate in the wind tunnel, near the wing base, so that boundary effects resulted in slower flow over the base than the tip. He measured $C_{L,max}$ close to 1.3, which is considerably higher than values derived without such a procedure and partly accounts for his conclusion that steady aerodynamic models may be adequate. Nachtigall (1981) used a propeller system to determine the forces on revolving model locust wings, but did not convert the results to appropriate coefficients.

The descent of samaras (such as sycamore keys) provides a case in which a steadily revolving, thin wing operates at high α. Azuma and Yasuda (1989) assume a $C_{L,max}$ of up to 1.8 in
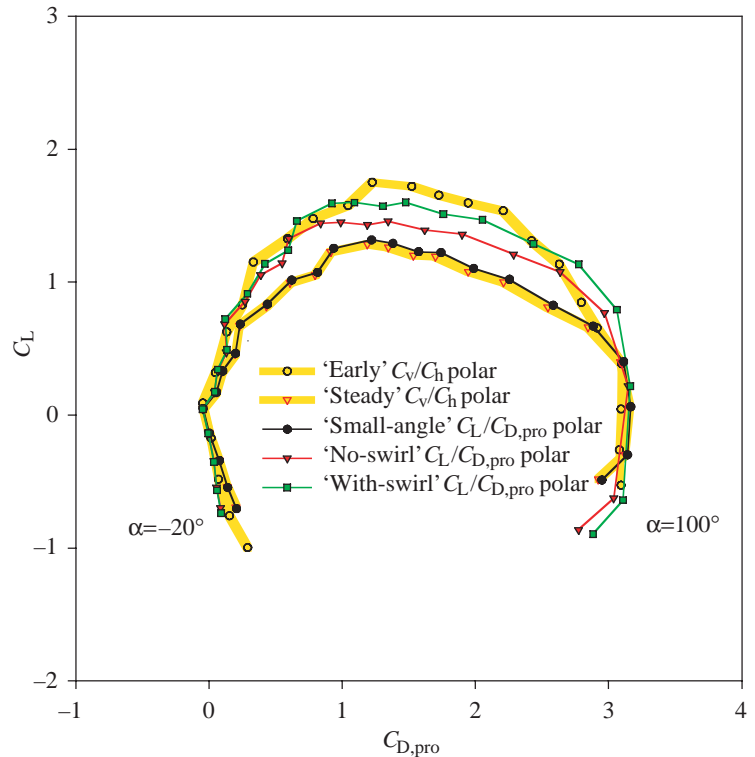

Fig. 10. Polar diagram showing results from three models for determining the profile drag coefficient $C_{D,pro}$ and the lift coefficient C_L from the 'steady' data represented by the lower yellow line. A good model would result in values close to, or slightly above, those of the 'early' conditions represented by the upper yellow line. Data are 'pooled' values for all wings in the 'leading-edge' series. C_h, horizontal force coefficient; C_v, vertical force coefficient; α, geometric angle of attack.

their models, but appear to find this value unremarkable. Norberg (1973) calculates high resultant force coefficients $[C_R=\sqrt{(C_h^2+C_v^2)}=1.7]$, but does comment that this 'stands out as a bit high'. Crimi (1996) has analysed the falling of 'samara-wing decelerators' (devices that control the descent rate of explosives) at much higher Reynolds numbers and found that the samara wings developed a considerably greater 'aerodynamic loading' than was predicted using their aerodynamic coefficients.

'Propeller' versus *'unsteady'* force coefficients

Although the steady propeller coefficients are of sufficient magnitude to account for the vertical force balance during hovering, this does not negate the possibility that unsteady mechanisms may be involved (Ellington, 1984a). Indeed, it would be surprising if unsteady mechanisms were not operating to some extent for flapping wings with low advance ratios. However, the results presented here suggest that the significance of unsteady mechanisms may be more limited to the control and manoeuvrability of flight (e.g. Ennos, 1989; Dickinson et al., 1999) than recently thought, although unsteady phenomena may have an important bearing on power requirements (Sane and Dickinson, 2001). Steady-state
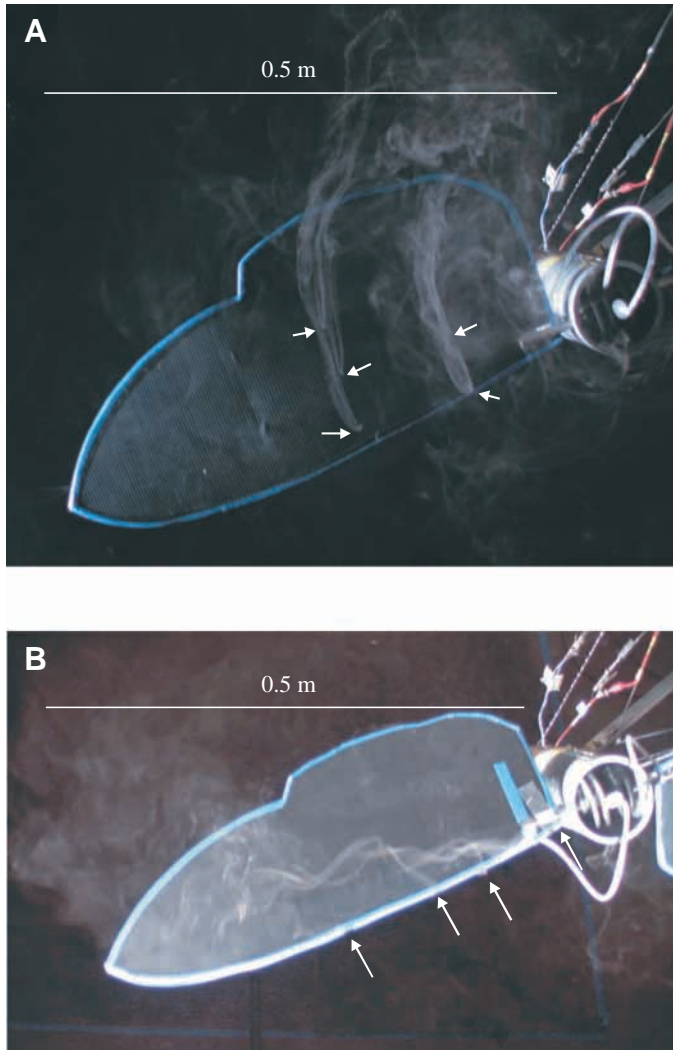
Fig. 11. Smoke flow over hawkmoth wings at α=0° (A) and α=35° (B) revolving steadily at 0.1 Hz. Smoke was released from various positions (marked with white arrows) on the leading edge and upper surface of the wings. At very low angles of attack, the smoke describes an approximately circular path as the wing revolves underneath. At higher angles of attack, a spiral leading-edge vortex and strong spanwise flow are visible. α, geometric angle of attack.
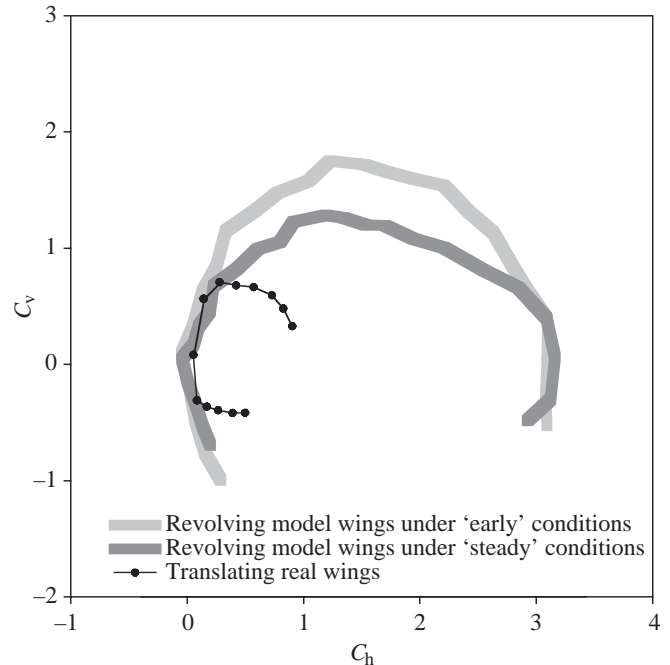

Fig. 12. Polar diagrams for real hawkmoth wings in steady translating flow and 'pooled' model hawkmoth wings in revolution under 'early' (upper grey line) and 'steady' (lower grey line) conditions. Data for hawkmoth in translational flow are taken from Willmott and Ellington (1997c) for a Reynolds number of 5560, and α ranges from –50 to 70° in 10° increments. C_h, horizontal force coefficient; C_v, vertical force coefficient; α, geometric angle of attack.

'propeller' coefficients (derived from revolving wings) may go much of the way towards accounting for the lift and power requirements of hovering and, while missing unsteady aspects, present the best opportunity for analysing power requirements in those insects, and those flight sequences, in which fine kinematic details are unknown.

The relationship between C_v and C_h for sharp, thin wings

The polar diagrams displayed in Fig. 12 show that horizontal force coefficients are also considerably higher for revolving wings. The relationship between vertical and horizontal force coefficients is of interest as it gives information on the cost (in terms of power due to aerodynamic drag) associated with a given vertical force (required to oppose weight in the case of hovering). Flow separation at the thin leading edge of the wing models described here must produce a quite different net pressure distribution from that found for conventional wings and is likely to be the cause of the C_v/C_h relationship described here.

Under two-dimensional, inviscid conditions, flow remains attached around the leading edge. This results in 'leading-edge suction': flow around the leading edge is relatively fast and so creates low pressure. The net pressure distribution results in a pure 'lift' force; drag due to the component of pressure forces acting on most of the upper wing surface is exactly counteracted by the leading-edge suction. This is true even for a thin flat-plate aerofoil: as the wing thickness approaches zero, the pressure due to leading-edge suction tends towards –∞, so that the leading-edge suction force remains finite. The pressure forces over the rest of the wing act normal to the wing surface. The horizontal component of the leading-edge suction force cancels the drag component of the pressure force over the rest of the wing. Under realistic, viscid conditions, this state can be achieved only by relatively thick wings with blunt leading edges operating at low angles of incidence.

Viscid flow around relatively thin aerofoils at high angles of incidence separates from the leading edge, and so there is no leading-edge suction. If viscous drag is also relatively small, the pressure forces acting normal to the wing surface dominate,

so the resultant force is perpendicular to the wing surface and not to the relative velocity. In the case of wings in revolution, the high vertical force coefficients can be attributed to the formation of leading-edge vortices. Leading-edge vortices are a result of leading-edge separation and so are directly associated with a loss of leading-edge suction; high vertical (or lift) forces due to leading-edge vortices must inevitably result in high horizontal (or drag) forces (Polhamus, 1971).

The dominance of the normal pressure force allows a 'normal force relationship' to be developed which relates vertical and horizontal force coefficients to C_R [$=\sqrt{(C_h^2+C_v^2)}$] and the geometric angle of attack α (see also Dickinson, 1996; Dickinson et al, 1999). Fig. 5 shows the forces acting on a wing element if the resultant force F_R' per unit span is dominated by normal pressure forces. This results, in terms of coefficients, in the relationships:

$$C_h = C_R\sin\alpha \qquad (24)$$

and

$$C_v = C_R\cos\alpha. \qquad (25)$$

These combine to produce the useful expressions:

$$\frac{C_v}{C_h} = \frac{1}{\tan\alpha} \qquad (26)$$

and

$$C_h = C_v\tan\alpha, \qquad (27)$$

which have the potential of being used to determine power requirements of hovering and slow flight (Usherwood, 2002).

Fig. 13 compares the measured vertical and horizontal coefficients with those predicted from the normal force relationship for the standard flat wing data. The success of the model for both 'early' and 'late' conditions suggests that pressure forces normal to the wing surface dominate the vertical and horizontal forces. At very low angles of incidence, it is likely that viscous forces largely comprise the horizontal (equivalent to drag) forces, but this cannot be determined from the data. At higher angles of incidence, however, C_h is clearly dominated by pressure forces acting perpendicular to the wing surface.

The trigonometry of the forces shown in Fig. 5 is such that the same physical arguments, this time with $C_R=\sqrt{(C_{D,pro}^2+C_L^2)}$, and the effective angle of attack α_r, result in:

$$C_{D,pro} = C_R\sin\alpha_r \qquad (28)$$

and

$$C_L = C_R\cos\alpha_r. \qquad (29)$$

From this:

$$\frac{C_L}{C_{D,pro}} = \frac{1}{\tan\alpha_r}, \qquad (30)$$

which may be used in power calculations based on the lift/drag frame of reference (Ellington, 1999).

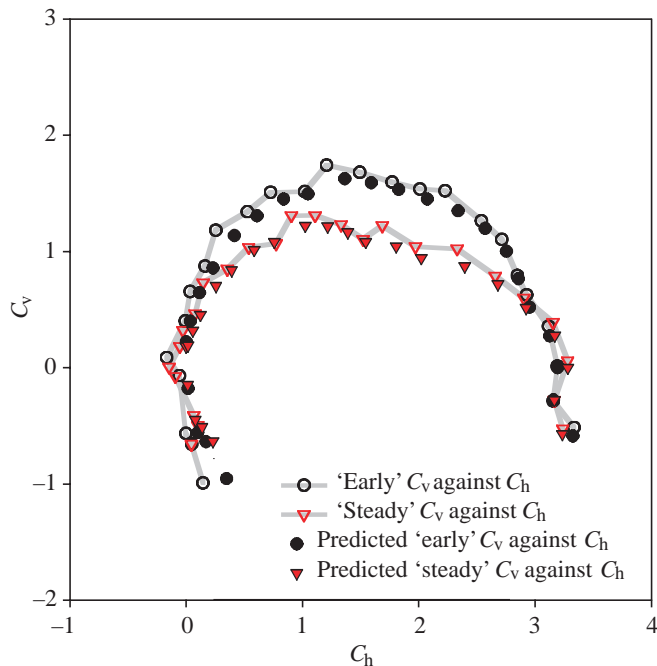This account of the pressure distribution over thin aerofoils and the normal force relationship should be applicable

Fig. 13. Polar diagram comparing measured horizontal (C_h) and vertical (C_v) force coefficients with those predicted from the normal force relationship for the standard, flat hawkmoth planform. α ranges from –20 to 100° in 5° increments. C_h, horizontal force coefficient; C_v, vertical force coefficient; α, geometric angle of attack.
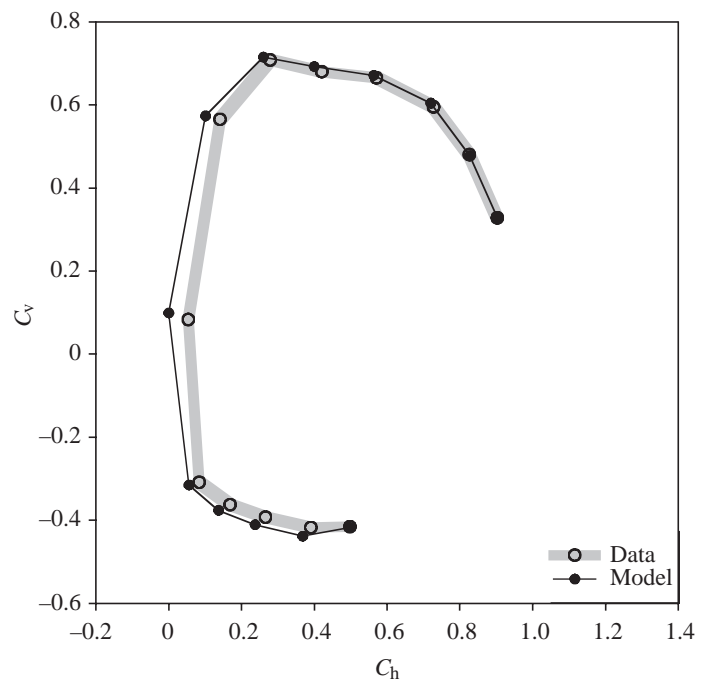
Fig. 14. Polar diagram showing the results of dividing the resultant force coefficient into horizontal and vertical coefficients using the 'normal force relationship'. The original data are for real hawkmoth wings in translational flow at a Reynolds number of 5560 (Willmott and Ellington, 1997c). α ranges from –50 to 70° in 10° increments. C_h, horizontal force coefficient; C_v, vertical force coefficient; α, geometric angle of attack.

whenever the flow separates from a sharp leading edge. Indeed, Fig. 14 shows that the division into vertical and horizontal force components using equations 24 and 25 fits very well for the real hawkmoth wings in translating flow, for which the leading-edge vortex is two-dimensional and unstable (Willmott and Ellington, 1997c). The model underestimates C_h at small angles of attack, but that is simply because skin friction is neglected. However, hawkmoth wings typically operate at much higher angles, at which the model fits the data very well for both translating and revolving wings.

The effects and implications of wing design

Leading-edge detail

The production of higher coefficients than would be expected in translating flow appears remarkably robust and is relatively consistent over quite a dramatic range of leading-edge styles. This may be surprising because the leading-edge characteristics of swept or delta wings are known to have effects on leading-edge vortex properties (Lowson and Riley, 1995) and are even used to delay or control the occurrence of leading-edge vortices at high angles of incidence. Wing features of some animals, such as the projecting bat thumb or the bird alula, may perform some role in leading-edge vortex delay or control analogous to wing fences and vortilons on swept-wing aircraft (see Barnard and Philpott, 1995). Such aircraft wings, and perhaps the analogous vertebrate wings, experience both conventional (attached) and detached (with a leading-edge vortex) flow regimes at different times and positions along the wing. However, the results presented here suggest that it is unlikely that very small-scale detail of leading edges, such as the serrations on the leading edges of dragonfly wings (e.g. Hertel, 1966), would influence the force coefficients for rapidly revolving wings. The peculiar microstructure of dragonfly wings may be more closely associated with their exceptional gliding performance (Wakeling and Ellington, 1997a).

Twist

The 'early' and 'steady' polar diagrams for the hawkmoth wing design with moderate (15°) twist are virtually identical to those for the flat wing design (Fig. 8). The only difference is that the zero-lift angle α_0 was approximately –10° for the twisted wing, so angles of incidence α' ranged from –30 to 90° instead of –20 to 100° as for the flat wings. Thus, the bottom left of the polar diagram was slightly extended and the bottom right shortened. The effect was even more pronounced for the highly twisted (32°) wing design. This design also showed a substantial reduction in the magnitude of the force coefficients at high angles of incidence, but this is readily explained: even when the wing base is set to a high angle of incidence, the tip of a highly twisted wing will be at a much lower angle.

Twist is desirable in propeller blades and has been assumed to be desirable for insects by analogy. The downwash angle ε is typically smaller towards the faster-moving tip of a propeller, so a lower angle of incidence α' is needed to give the same effective angle of incidence α_r' (=$\alpha'-\varepsilon$). Thus, a twisted blade allows some optimal effective angle of incidence to be maintained at each radial station despite the varying effects of downwash. However, what this optimal effective angle of incidence should be is unclear for insects. These revolving, low-Re wings show no features of conventional stall; changes from high C_v to high C_h with increasing angle of incidence can be related entirely to the normal pressure force and not to the sudden development of a stalled wake. So it is not, presumably, stall that is being avoided with the twisted wing.

The characteristic normally optimised in propeller design is the 'aerodynamic efficiency' or lift-to-drag ratio. This occurs at α_r' well below 10° for conventional propellers and at α ($\approx\alpha_r'$ at these small angles) around 10° for the translating hawkmoth wings (Willmott and Ellington, 1997c). The maximum lift-to-drag ratio could not be determined in this study because of noise in the torque transducer at small angles of incidence, but it is reasonable to suppose that the optimal α_r' for aerodynamic efficiency is low, probably below 10°. This is certainly below the angles used by hawkmoths, in which α ranges from 21 to 74° (Willmott and Ellington, 1997b) or by many hovering insects: Ellington (1984c) gives $\alpha=35°$ as a typical value. So, twist is not maintaining an α_r' along the wing that maximises the lift-to-drag ratio. The angles of attack for hovering insects suggest that a compromise between high lift and a reasonably small drag might be more important than maximising the lift-to-drag ratio. They operate near the upper left corner of the polar diagram, and the observed moderate wing twists might sustain the appropriate α_r' along the wing. However, it must be emphasised that the polar diagrams for the flat and moderately twisted wings were almost identical. The same point on the polar diagram could be attained by either wing design simply by altering the geometric angle of attack, so there are no clear benefits to the twisted wing.

Less direct aerodynamic functions of twist should also be considered. Ennos (1988) shows that camber may be produced through wing twist in many wing designs, so any aerodynamic advantages of camber might drive the evolution of twisted wings. It is also possible that twisting may have no aerodynamic role whatever or may even be aerodynamically disadvantageous. The null hypothesis for this discussion should be that wing twist is just a structural inevitability for ultra-light wings experiencing rapidly changing aerodynamic and inertial forces. Twist may simply occur as a result of rotational inertia during pronation and supination and be maintained because of aerodynamic loading on a slightly flimsy wing. The lack of twist in flapping *Drosophila* wings has been explained by the higher relative torsional stiffness of smaller wings (Ellington, 1984c). If twisting had aerodynamic advantages, the evolution of more flexible materials (which, if anything, should be less costly) might be expected. Of course, these arguments are confounded in many aspects, including *Re*. However, it is difficult for any description of an aerodynamic function of twist to account for the purpose of wings twisted in the opposite sense, where the base operates at lower α than the tip. This appears to be the case for *Phormia regina* (Nachtigall, 1979).

Camber

Fig. 9 agrees with results on the performance of two-dimensional model *Drosophila* wings in unsteady flow (Dickinson and Götz, 1993); any changes in the aerodynamic properties of model hawkmoth wings due to camber are slight. Shifts in maximum C_h or C_v appear to be within the experimental error, so these trends should not be put down to aerodynamic effects. The similarities of the polar diagrams show that camber provides little improvement in lift-to-drag ratios at relevant angles of incidence.

Camber is beneficial in conventional wings because it increases the angle of incidence gradually across the chord. This shape deflects air downwards gradually, and the abrupt and undesirable breaking away of flow from the upper surface is avoided. So, the conventional reasoning behind the benefits of cambered wings to insects appears flawed: flapping insect wings use flow separation at the leading edge as a fundamental part of lift generation. A reasonable analogy exists with aeroplane wings. The thin wings of a landing Tornado jet use leading- and trailing-edge flaps to increase wing camber, maintaining attached flow and allowing higher lift coefficients than would otherwise be possible. Concorde, however, uses the high force coefficients associated with leading-edge vortices created by flow separation from the sharp, swept leading edges: no conventional leading-edge flaps are used because flow separation from the leading edge is intentional.

Camber still has a role in improving the aerodynamic performance of gliding wings, but any beneficial aerodynamic effects for flapping insect wings will require experimental evidence and not analogy with conventional wings designed (or adapted) for attached flow.

Accounting for differences between 'early' and 'steady' propeller coefficients

Fig. 4 and Figs 6–9 show that there is a considerable change in force production between 'early' and 'steady' conditions. There are two possible reasons for this change. First, the wings cause an induced flow in steady revolution that is absent at the start, and this decreases the effective angle of incidence. Second, there may be a fundamental change in aerodynamics due, for instance, to the shedding of the leading-edge vortex (and a resulting stall), as is seen for translating wings (Dickinson and Götz, 1993). Simple accounts are taken of the induced downwash in the calculation of $C_{D,pro}$ and C_L from steady coefficients (Fig. 10). Below $\alpha'=50°$, the downwash alone appears to account for the shift between 'early' and 'steady' propeller coefficients; the calculated values of $C_{D,pro}$ and C_L fit the observed values of $C_{h,early}$ and $C_{v,early}$ well. Also, the observation (Fig. 11) that leading-edge vortices can be maintained during steady revolution supports the view that the shift in propeller coefficients can be accounted for by the effects of downwash alone, without a fundamental change in aerodynamics.

At very high α', the downwash models for determining $C_{D,pro}$ and C_L provide poorer results. A change in the value of $\overline{w}_0$ at high α' can improve the fit of $C_{D,pro}$ and C_L to $C_{h,early}$

and $C_{v,early}$: both k_{ind} and R (separation at the wing tip may reduce the effective wing length) in equation 11 may be altered. However, varying correction factors in the high α' range without *a priori* justification (such as more accurate flow visualisation) limits the possibility of aerodynamic inferences. Both fundamental changes in aerodynamics and failure of the Rankine–Froude actuator disc model for calculating induced downwash are also reasonable explanations for part of the shift in propeller coefficients between 'early' and 'steady' conditions at very high α'. The appearance of trailing-edge vortices at high angles of incidence may be a relevant aerodynamic shift and may also account for the relatively high force values for $45°<\alpha<75°$. An aerodynamic change due to a shift in the position of the vortex core breakdown is particularly worthy of consideration. Ellington et al. (1996) and Van den Berg and Ellington (1997b) noted that the core of the spiral leading-edge vortex broke down at approximately two-thirds of the wing length, resulting in a loss of lift in outer wing regions. Liu et al. (1998) postulated that this breakdown is due to the adverse pressure gradient over the upper wing surface caused by the tip vortex. The development of the full vortex wake with its associated radial inflow over the wings might well shift the position of vortex breakdown inwards under 'steady' conditions at higher α', producing a quantitative reduction in the lift coefficient compared with the 'early' state.

List of symbols

AR	aspect ratio
c	wing chord
$C_{D,pro}$	profile drag coefficient
C_h	horizontal force coefficient
C_L	lift coefficient
C_R	resultant force coefficient
C_v	vertical force coefficient
D_{pro}	profile drag
D_{pro}'	Profile drag on wing element
F_h	horizontal force
F_h'	Horizontal force on wing element
F_v	vertical force
F_v'	Vertical force on wing element
F_R'	single resultant force
k_{ind}	correction factor for induced power
L	lift
L'	Lift on wing element
Q	torque
r	radial position along the wing
$\hat{r}_2(S)$	non-dimensional second moment of area
$\hat{r}_3(S)$	non-dimensional third moment of area
R	wing length
Re	Reynolds number
S	total wing area (for two wings)
S_2	second moment of area for both wings
S_3	third moment of area for both wings
U	velocity of a wing element
U_r	relative velocity of air at a wing element

V	velocity
w_0	vertical component of induced downwash velocity
α	geometric angle of attack
α_r	effective angle of attack
α_0	zero-lift angle of attack
α'	angle of incidence
α_r'	effective angle of incidence
ε	downwash angle
ρ	density of air
Ω	angular velocity of the propeller

Subscripts

early	before propeller wake has developed (e.g. $C_{v,early}$)
max	maximum value (e.g. $C_{L,max}$)
r	relating to a wing element (e.g. c_r)
steady	after propeller wake has developed (e.g. $C_{v,steady}$)

References

Ashill, P. R., Riddle, G. L. and Stanley, M. J. (1995). Separation control on highly-swept wings with fixed or variable camber. *Aeronaut. J.* **October**, 317–327.

Azuma, A. and Yasuda, K. (1989). Flight performance of rotary seeds. *J. Theor. Biol.* **138**, 23–53.

Barnard, R. H. and Philpott, D. R. (1995). *Aircraft Flight*. Harlow: Longman.

Brackenbury, J. H. (1995). *Insects in Flight*. London: Cassel.

Cloupeau, M., Devillers, J. F. and Devezeaux, D. (1979). Direct measurements of instantaneous lift in desert locust: comparison with Jensen's experiments on detached wings. *J. Exp. Biol.* **80**, 1–15.

Crimi, P. (1996). Finite element analysis of a samara-wing decelerator. *J. Aircraft* **33**, 793–802.

Dalton, S. (1977). *The Miracle of Flight*. London: Sampson Low.

Dickinson, M. H. (1996). Unsteady mechanisms of force generation in aquatic and aerial locomotion. *Am. Zool.* **36**, 536–554.

Dickinson, M. H. and Götz, K. G. (1993). Unsteady aerodynamic performance of model wings at low Reynolds numbers. *J. Exp. Biol.* **174**, 45–64.

Dickinson, M. H., Lehmann, F.-O. and Sane, S. P. (1999). Wing rotation and the aerodynamic basis of insect flight. *Science* **284**, 1954–1960.

Dudley, R. (1991). Biomechanics of flight in neotropical butterflies: aerodynamics and mechanical power requirements. *J. Exp. Biol.* **159**, 335–357.

Dudley, R. and Ellington, C. P. (1990). Mechanics of forward flight in bumblebees. II. Quasi-steady lift and power requirements. *J. Exp. Biol.* **148**, 53–88.

Ellington, C. P. (1984a). The aerodynamics of hovering insect flight. I. The quasi-steady analysis. *Phil. Trans. R. Soc. Lond. B* **305**, 1–15.

Ellington, C. P. (1984b). The aerodynamics of hovering insect flight. II. Morphological parameters. *Phil. Trans. R. Soc. Lond. B* **305**, 17–40.

Ellington, C. P. (1984c). The aerodynamics of hovering insect flight. III. Kinematics. *Phil. Trans. R. Soc. Lond. B* **305**, 41–78.

Ellington, C. P. (1984d). The aerodynamics of hovering insect flight. IV. Aerodynamic mechanisms. *Phil. Trans. R. Soc. Lond. B* **305**, 79–113.

Ellington, C. P. (1984e). The aerodynamics of hovering insect flight. V. A vortex theory. *Phil. Trans. R. Soc. Lond. B* **305**, 115–144.

Ellington, C. P. (1984f). The aerodynamics of hovering insect flight. VI. Lift and power requirements. *Phil. Trans. R. Soc. Lond. B* **305**, 145–181.

Ellington, C. P. (1999). The novel aerodynamics of insect flight: applications to micro-air vehicles. *J. Exp. Biol.* **202**, 3439–3448.

Ellington, C. P., Van den Berg, C., Willmott, A. P. and Thomas, A. L. R. (1996). Leading-edge vortices in insect flight. *Nature* **384**, 626–630.

Ennos, A. R. (1988). The importance of torsion in the design of insect wings. *J. Exp. Biol.* **140**, 137–160.

Ennos, A. R. (1989). The kinematics and aerodynamics of the free flight of some Diptera. *J. Exp. Biol.* **142**, 49–85.

Hertel, H. (1966). *Structure, Form, Movement*. New York: Reinhold.

Jensen, M. (1956). Biology and physics of locust flight. III. The aerodynamics of locust flight. *Phil. Trans. R. Soc. Lond. B* **239**, 511–552.

Liu, H., Ellington, C. P., Kawachi, K., Van den Berg, C. and Willmott, A. P. (1998). A computational fluid dynamic study of hawkmoth hovering. *J. Exp. Biol.* **201**, 461–477.

Lowson, M. V. and Riley, A. J. (1995). Vortex breakdown control by delta wing geometry. *J. Aircraft* **32**, 832–838.

Maxworthy, T. (1979). Experiments on the Weis-Fogh mechanism of lift generation by insects in hovering flight. Part 1. Dynamics of the 'fling'. *J. Fluid Mech.* **93**, 47–63.

Nachtigall, W. (1977). Die aerodynamische Polare des Tipula-Flügels und eine Einrichtung zur halbautomatischen Polarenaufnahme. In *The Physiology of Movement; Biomechanics* (ed. W. Nachtigall), pp. 347–352. Stuttgart: Fischer.

Nachtigall, W. (1979). Rasche Richtungsänderungen und Torsionen schwingender Fliegenflügel und Hypothesen über zugeordnete instationäre Strömungseffekte. *J. Comp. Physiol.* **133**, 351–355.

Nachtigall, W. (1981). Der Vorderflügel grosser Heuschrecken als Luftkrafterzeuger. I. Modellmessungen zur aerodynamischen Wirkung unter schiedlicher Flügel profile. *J. Comp. Physiol.* **142**, 127–134. [Locust wing models in parallel and rotating flow].

Newman, B. G., Savage, S. B. and Schouella, D. (1977). Model tests on a wing section of an *Aeschna* dragonfly. In *Scale Effects in Animal Locomotion* (ed. T. J. Pedley), pp. 445–477. London: Academic Press.

Norberg, R. Å. (1972). Flight characteristics of two plume moths, *Alucita pentadactyla* L. and *Orneodes hexadactyla* L. (Microlepidoptera). *Zool. Scripta* **1**, 241–246.

Norberg, R. Å. (1973). Autorotation, self-stability and structure of single-winged fruits and seeds (samaras) with comparative remarks on animal flight. *Biol. Rev.* **48**, 561–596.

Okamoto, M., Yasuda, K. and Azuma, A. (1996). Aerodynamic characteristics of dragonfly wings and body. *J. Exp. Biol.* **199**, 281–294.

Osborne, M. F. M. (1951). Aerodynamics of flapping flight with application to insects. *J. Exp. Biol.* **28**, 221–245.

Polhamus, E. C. (1971). Predictions of vortex lift characteristics by a leading-edge suction analogy. *J. Aircraft* **8**, 193–198.

Sane, S. P. and Dickinson, M. H. (2001). The control of flight force by a flapping wing: lift and drag production. *J. Exp. Biol.* **204**, 2607–2626.

Stepniewski, W. Z. and Keys, C. N. (1984). *Rotary-Wing Aerodynamics*. New York: Dover.

Usherwood, J. R. (2002). Aerodynamics and energetics of animal flight based on propeller models. PhD thesis, Cambridge University.

Van den Berg, C. and Ellington, C. P. (1997a). The vortex wake of a 'hovering' model hawkmoth. *Phil. Trans. R. Soc. Lond. B* **352**, 317–328.

Van den Berg, C. and Ellington, C. P. (1997b). The three-dimensional leading-edge vortex of a 'hovering' model hawkmoth. *Phil. Trans. R. Soc. Lond. B* **352**, 329–340.

Vogel, S. (1967a). Flight in *Drosophila*. II. Variations in stroke parameters and wing contour. *J. Exp. Biol.* **46**, 383–392.

Vogel, S. (1967b). Flight in *Drosophila*. III. Aerodynamic characteristics of fly wings and wing models. *J. Exp. Biol.* **46**, 431–443.

Wakeling, J. M. and Ellington, C. P. (1997a). Dragonfly flight. I. Gliding flight and steady-state aerodynamic forces. *J. Exp. Biol.* **200**, 543–556.

Wakeling, J. M. and Ellington, C. P. (1997b). Dragonfly flight. III. Lift and power requirements. *J. Exp. Biol.* **200**, 583–600.

Weis-Fogh, T. (1973). Quick estimates of flight fitness in hovering animals, including novel mechanisms for lift production. *J. Exp. Biol.* **59**, 169–230.

Wells, D. J. (1993). Muscle performance in hovering hummingbirds. *J. Exp. Biol.* **178**, 39–57.

Willmott, A. P. and Ellington, C. P. (1997a). Measuring the angle of attack of beating insect wings: robust three-dimensional reconstruction from two-dimensional images. *J. Exp. Biol.* **200**, 2693–2704.

Willmott, A. P. and Ellington, C. P. (1997b). The mechanics of flight in the hawkmoth *Manduca sexta*. I. Kinematics of hovering and forward flight. *J. Exp. Biol.* **200**, 2705–2722.

Willmott, A. P. and Ellington, C. P. (1997c). The mechanics of flight in the hawkmoth *Manduca sexta*. II. Aerodynamic consequences of kinematic and morphological variation. *J. Exp. Biol.* **200**, 2723–2745.

Willmott, A. P., Ellington, C. P. and Thomas, A. L. R. (1997). Flow visualization and unsteady aerodynamics in the flight of the hawkmoth, *Manduca sexta. Phil. Trans. R. Soc. Lond. B* **352**, 303–316.

Wootton, R. J. (1981). Support and deformability in insect wings. *J. Zool., Lond.* **193**, 447–468.

Wootton, R. J. (1991). The functional morphology of the wings of Odonata. *Adv. Odonatol.* **5**, 153–169.

Wootton, R. J. (1992). Functional morphology of insect wings. *Annu. Rev. Entomol.* **37**, 113–140.

Wootton, R. J. (1993). Leading edge sections and asymmetric twisting in the wings of flying butterflies (Insects, Papilionoidea). *J. Exp. Biol.* **180**, 105–117.

Wootton, R. J. (1995). Geometry and mechanics of insect hindwing fans – a modelling approach. *Proc. R. Soc. Lond. B* **262**, 181–187.